Applied Numerical Mathematics 151 (2020) 263–281

Contents lists available at ScienceDirect

Applied Numerical Mathematics

www.elsevier.com/locate/apnum

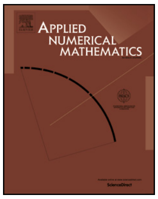

Efficient and energy stable method for the Cahn-Hilliard phase-field model for diblock copolymers

Jun Zhang [a,b], Chuanjun Chen [c,*], Xiaofeng Yang [d]

[a] Guizhou Key Laboratory of Big Data Statistics Analysis, Guizhou University of Finance and Economics, Guiyang, Guizhou, 550025, China
[b] Computational Mathematics Research Center, Guizhou University of Finance and Economics, Guiyang, Guizhou 550025, China
[c] School of Mathematics and Information Sciences, Yantai University, Yantai 264005, China
[d] Department of Mathematics, University of South Carolina, Columbia, SC 29208, USA

ARTICLE INFO

Article history:
Received 5 June 2019
Received in revised form 2 October 2019
Accepted 8 December 2019
Available online 7 January 2020

Keywords:
Phase-field
S-SAV
Diblock copolymer
Cahn-Hilliard
Second order
Unconditional energy stability

ABSTRACT

In this paper, we consider numerical approximations to solving the Cahn-Hilliard phase field model for diblock copolymers. We combine the recently developed SAV (scalar auxiliary variable) approach with the stabilization technique to arrive at a novel stabilized-SAV method, where a crucial linear stabilization term is added to enhancing the stability and keeping the required accuracy while using the large time steps. The scheme is very easy-to-implement and fast in the sense that one only needs to solve two decoupled fourth-order biharmonic equations with constant coefficients at each time step. We further prove the unconditional energy stability of the scheme rigorously. Through the comparisons with some other prevalent schemes like the fully-implicit, convex-splitting, and non-stabilized SAV scheme for some benchmark numerical examples in 2D and 3D, we demonstrate the stability and the accuracy of the developed scheme numerically.

1. Introduction

A diblock copolymer is a polymer consisting of two types of monomers which are arranged such that there is a chain of each monomer, and those two chains are grafted together to form a single copolymer chain. Some of the common shapes of diblock copolymers that have been observed experimentally are lines (lamellar), hexagonal cylinders, gyroids, and stacked balls (body-centered-cubic, BCC for short). Copolymerization is used to modify the properties of manufactured plastics to meet specific needs, for example, to reduce crystallinity, modify glass transition temperature, control wetting properties or to improve solubility, see [17,22].

In this paper, we consider numerical approximations for solving a phase-field model for diblock copolymers where a scalar phase field variable is used to denote the difference between the local volume fractions of two monomers, cf. [2,6,12,21,28,30]. The governing PDE system is derived by using the Cahn-Hilliard dynamics, i.e., the total free energy (called as Ohta-Kawasaki free energy) is minimized in H^{-1} Sobolev space since the phase field variable represents the difference of the local volume fractions of the two constituent monomers which is expected to be conserved with the time. To design fast, stable, and accurate time stepping method for the phase-field related model that usually follows the energy dissipation law, the main challenging issue is to find proper discretization for the nonlinear term. For this particular model, the

---

* Corresponding author.
E-mail addresses: jzhang@mail.gufe.edu.cn (J. Zhang), cjchen@ytu.edu.cn (C. Chen), xfyang@math.sc.edu (X. Yang).

https://doi.org/10.1016/j.apnum.2019.12.006

only nonlinear term is the cubic polynomial term from the double-well potential. In fact, there are quite many prevalent temporal discretization methods to handling the nonlinear term for phase-field models, for instances, the fully-explicit [25], fully-implicit [10], convex-splitting [9,18,19,26], stabilized-explicit [13,20,25], Invariant Energy Quadratization (IEQ) [3,29, 31–33,35–37], Scalar Auxiliary variable (SAV) [4,5,27], and a variety of other type methods [14–16,23], etc. Some methods mentioned above are provably energy stable, i.e., the discrete solution can preserve the energy dissipation law at the discrete level. However, when the mobility parameter or the time step is large, the obtained linear/linearized system could be ill-conditioned thereby even those provably energy stable schemes like convex-splitting, IEQ, or SAV method can still blow up, or lead to very costly iterations, cf. the accuracy tests shown in Fig. 4.2-Fig. 4.3.

The aim of this paper is to develop a numerical scheme that is fast (free of iterations), stable, and second-order accurate. To this end, we combine the SAV approach with the stabilization technique that brings up a novel stabilized-SAV (S-SAV) approach, where an extra linear stabilization term is added to enhancing the stability and thus allowing large time steps while keeping the required accuracy. Meanwhile, the implementation procedure for the developed S-SAV method is very simple, in which, we first transform the total free energy integral into a quadratic function of a new, scalar auxiliary variable via a change of variables. Then, for the reformulated model in terms of the new variable, we treat all nonlinear terms in a semi-explicit way. Due to the specialty of the new variable that is non-local type formally, one only needs to solve two decoupled, linear biharmonic equations with constant coefficients at each time step. In addition to presenting the rigorous proof of the unconditional energy stability, we further demonstrate the stability and accuracy numerically through the comparisons with some prevalent schemes like the fully-implicit, convex-splitting, and non-stabilized SAV schemes for a number of classical benchmark numerical examples in 2D and 3D.

The rest of the paper is organized as follows. In Section 2, we give a brief introduction of the governing PDE system for the phase-field diblock copolymer model. In Section 3, we develop the numerical scheme with second-order temporal accuracy to solving this model. Various 2D and 3D numerical experiments are given in Section 4 to show the accuracy and efficiency of the proposed numerical scheme. Finally, some concluding remarks are given in Section 5.

2. Model equations

We now give a brief introduction to the diblock copolymer model. Assuming a system consists of molecules of two monomers, where the state of the system is described by the local volume fraction of these two components, $\phi(\boldsymbol{x},t)$ with $\boldsymbol{x}\in\Omega^d, d=2,3$ and time t. The phenomenological mesoscopic dynamic equation that relates a temporal change of $\phi(\boldsymbol{x},t)$ is governed by the following Cahn-Hilliard equation (cf. [1,7,8,11]):

$$\begin{cases} \phi_t = M\Delta w, \\ w = \dfrac{\delta E(\phi)}{\delta\phi}, \end{cases} \tag{2.1}$$

where M is the mobility parameter, $E(\phi)$ is a coarse-grained free energy functional that is given as

$$E(\phi)=\int\limits_\Omega \Big(\frac{\epsilon^2}{2}|\nabla\phi|^2+F(\phi)\Big)d\boldsymbol{x}+\frac{\alpha\epsilon^2}{2}\int\limits_\Omega\int\limits_\Omega G(\boldsymbol{x}-\boldsymbol{y})(\phi(\boldsymbol{x})-\bar\phi)(\phi(\boldsymbol{y})-\bar\phi)d\boldsymbol{x}d\boldsymbol{y}, \tag{2.2}$$

where ϵ is the gradient energy coefficient, the function $F(\phi)=\frac{1}{4}(\phi^2-1)^2$ is the bulk Ginzburg-Landau double well potential, $\bar\phi(t):=\frac{1}{|\Omega|}\int_\Omega\phi(\boldsymbol{x},t)d\boldsymbol{x}$, G is the Green's function such that

$$G(\boldsymbol{x}-\boldsymbol{y})=-\delta(\boldsymbol{x}-\boldsymbol{y}), \tag{2.3}$$

with the periodic boundary condition, δ is a Dirac delta function, α is the nonlocal positive parameter to characterizes the nonlocal potential and the molecular chain length, and the last term in (2.2) is the so-called nonlocal Ohta-Kawasaki functional.

We define the inverse Laplace operator $\psi=(-\Delta)^{-1}\phi$ as

$$\begin{cases} -\Delta\psi=\phi, \\ \displaystyle\int\limits_\Omega\psi d\boldsymbol{x}=0, \end{cases} \tag{2.4}$$

with the periodic boundary conditions, where $\phi\in L_0^2(\Omega):=\{\phi\in L^2(\Omega):\int_\Omega\phi d\boldsymbol{x}=0\}$. By taking the total free energy described in (2.2), the PDE system (2.1) turns into

$$\phi_t=M\Delta w, \tag{2.5}$$

$$w=-\epsilon^2\Delta\phi+f(\phi)+\alpha\epsilon^2\psi, \tag{2.6}$$

$$\psi=(-\Delta)^{-1}(\phi-\bar\phi), \tag{2.7}$$

or an equivalent form as

$$\phi_t = M(\Delta\mu - \alpha\epsilon^2(\phi - \bar{\phi})), \tag{2.8}$$

$$\mu = -\epsilon^2\Delta\phi + f(\phi), \tag{2.9}$$

where $f(\phi) = F'(\phi) = \phi^3 - \phi$.

Without the loss of generality, we adopt the periodic boundary condition to remove all complexities associated with the boundary integrals in this study. We remark that the boundary conditions can also be the no-flux type as

$$\partial_{\mathbf{n}}\phi|_{\partial\Omega} = \nabla w \cdot \mathbf{n}|_{\partial\Omega} = 0, \tag{2.10}$$

for (2.5)-(2.7), or

$$\partial_{\mathbf{n}}\phi|_{\partial\Omega} = \nabla\mu \cdot \mathbf{n}|_{\partial\Omega} = 0, \tag{2.11}$$

for (2.8)-(2.9), where $\mathbf{n}$ is the outward normal of the computational domain Ω. All numerical analysis in this paper can be carried out to the no-flux boundary conditions without any further difficulties.

The model (2.5)-(2.7) follows the energy dissipation law. By taking the L^2 inner product of (2.5) with $-w$, and of (2.6) with ϕ_t, performing integration by parts, and taking summation of the two equalities, we obtain

$$\frac{d}{dt}\int_{\Omega}(\frac{\epsilon^2}{2}|\nabla\phi|^2 + F(\phi))d\boldsymbol{x} + \alpha\epsilon^2(\psi, \phi_t) = -M\|\nabla w\|^2. \tag{2.12}$$

We rewrite (2.7) as the form (2.4), i.e., $-\Delta\psi = \phi - \bar{\phi}$ with $\int_{\Omega}\psi d\boldsymbol{x} = 0$, and then take the time derivative to obtain

$$-\Delta\psi_t = \phi_t - \bar{\phi}_t. \tag{2.13}$$

By taking the L^2 inner product of the above formula with $\alpha\epsilon^2\psi$, we obtain

$$\frac{d}{dt}\int_{\Omega}\frac{\alpha\epsilon^2}{2}|\nabla\psi|^2 d\boldsymbol{x} = \alpha\epsilon^2(\psi, \phi_t), \tag{2.14}$$

where the zero mean property of ψ is used. By combining (2.12) and (2.14), we obtain

$$\frac{d}{dt}E(\phi, \psi) = -M\|\nabla w\|^2, \tag{2.15}$$

where

$$E(\phi, \psi) = \int_{\Omega}(\frac{\epsilon^2}{2}|\nabla\phi|^2 + F(\phi) + \frac{\alpha\epsilon^2}{2}|\nabla\psi|^2)d\boldsymbol{x}. \tag{2.16}$$

3. Numerical schemes

We develop a second-order accurate and provably unconditionally energy stable scheme by combining the SAV approach [5,27] with the stabilization technique, that arrives at the stabilized-SAV approach. An extra linear stabilization term is particularly efficient to enhancing the energy stability while keeping the computation fast with the required accuracy.

3.1. Stabilized-SAV scheme

We define a scalar, auxiliary variable $u(t)$ as follows:

$$u(t) = \sqrt{\int_{\Omega} F(\phi)d\boldsymbol{x} + B}, \tag{3.1}$$

where B is any constant that ensures the radicand positive (in all numerical examples, we let $B = 1$). Thus the total free energy (2.16) can be rewritten as

$$E(u, \phi, \psi) = \int_{\Omega}(\frac{\epsilon^2}{2}|\nabla\phi|^2 + \frac{\alpha\epsilon^2}{2}|\nabla\psi|^2)d\boldsymbol{x} + u^2 - B. \tag{3.2}$$

By taking the time derivative for the new variable $u(t)$, we can rewrite the system (2.5)-(2.7) to be the following system in terms of (ϕ, u, w, ψ),

$$\phi_t = M\Delta w, \tag{3.3}$$

$$w = -\epsilon^2\Delta\phi + uH + \alpha\epsilon^2\psi, \tag{3.4}$$

$$u_t = \frac{1}{2}\int\limits_{\Omega} H(\phi)\phi_t d\boldsymbol{x}, \tag{3.5}$$

$$\psi = (-\Delta)^{-1}(\phi - \bar{\phi}), \tag{3.6}$$

where

$$H(\phi) = \frac{f(\phi)}{\sqrt{\int_\Omega F(\phi)d\boldsymbol{x} + B}}. \tag{3.7}$$

The transformed system (3.3)-(3.6) forms a closed PDE system with the following initial conditions,

$$\begin{cases} \phi(t=0) = \phi^0, \\ u(t=0) = \sqrt{\int\limits_{\Omega} F(\phi^0)d\boldsymbol{x} + B}. \end{cases} \tag{3.8}$$

The system (3.3)-(3.6) also preserves the energy dissipative law. By taking the L^2 inner product of (3.3) with $-w$, of (3.4) with ϕ_t, and multiplying (3.4) with $2u$, performing integration by parts, taking the time derivative for (3.6) and taking the L^2 product with ψ, and summing all equalities up, we can obtain the energy dissipation law as

$$\frac{d}{dt}E(u, \phi, \psi) = -M\|\nabla\mu\|^2 \le 0. \tag{3.9}$$

Let $\delta t > 0$ be a time step size and set $t^n = n\delta t$ for $0 \le n \le N$ with $T = N\delta t$. We also denote the L^2 inner product of any two spatial functions $\phi(\boldsymbol{x})$ and $\psi(\boldsymbol{x})$ by $(\phi(\boldsymbol{x}), \psi(\boldsymbol{x})) = \int_\Omega \phi(\boldsymbol{x})\psi(\boldsymbol{x})d\boldsymbol{x}$, and the L^2 norm of the function $\phi(\boldsymbol{x})$ by $\|\phi\|^2 = (\phi, \phi)$. Let ψ^n denote the numerical approximation to $\psi(\cdot, t)|_{t=t^n}$ for any function ψ.

We now construct a numerical scheme based on the second-order backward differentiation formula (BDF2) for solving the system (3.3)-(3.6), that reads as follows.

Assuming ϕ^n, u^n and ϕ^{n-1}, u^{n-1} are known, we update ϕ^{n+1}, u^{n+1} by solving

$$\frac{3\phi^{n+1} - 4\phi^n + \phi^{n-1}}{2M\delta t} = \Delta w^{n+1}, \tag{3.10}$$

$$w^{n+1} = -\epsilon^2\Delta\phi^{n+1} + u^{n+1}H^{*,n+1} + \alpha\epsilon^2\psi^{n+1} + S(\phi^{n+1} - \phi^{*,n+1}), \tag{3.11}$$

$$3u^{n+1} - 4u^n + u^{n-1} = \frac{1}{2}\int\limits_{\Omega} H^{*,n+1}(3\phi^{n+1} - 4\phi^n + \phi^{n-1})d\boldsymbol{x}, \tag{3.12}$$

$$\psi^{n+1} = -(\Delta^{-1})(\phi^{n+1} - \bar{\phi}^{n+1}), \tag{3.13}$$

where

$$\phi^{*,n+1} = 2\phi^n - \phi^{n-1},\ H^{*,n+1} = H(\phi^{*,n+1}), \tag{3.14}$$

and S is a positive stabilizing parameter.

Remark 3.1. We add a second-order linear stabilizer (associated with S) in the scheme to balance the explicit treatment of the nonlinear term $f(\phi)$ in term H. Therefore the magnitude of S should be around $\|\phi\|_{L^\infty}$ heuristically. Numerical examples show that this stabilizer is crucial to enhancing the stability while keeping the required accuracy, cf. the comparisons with the non-stabilized SAV (i.e., the scheme (3.10)-(3.13) but with $S = 0$), fully-implicit, and convex-splitting approaches shown in Fig. 4.1-Fig. 4.3.

Remark 3.2. To initiate the second-order scheme (3.10)-(3.13), we need the values of ϕ^1, u^1, that can be obtained by the following similar first-order scheme based on backward Euler formulation that reads as,

$$\frac{\phi^1-\phi^0}{M\delta t} = \Delta w^1, \tag{3.15}$$

$$w^1 = -\epsilon^2\Delta\phi^{n+1} + u^1 H^0 + \alpha\epsilon^2\psi^1 + S(\phi^1-\phi^0), \tag{3.16}$$

$$u^1 - u^0 = \frac{1}{2}\int_\Omega H^0(\phi^1-\phi^0)d\boldsymbol{x}, \tag{3.17}$$

$$\psi^1 = -(\Delta^{-1})(\phi^1-\bar{\phi}^1), \tag{3.18}$$

where $H^0 = H(\phi^0)$.

Apparently, we arrive at a linear but nonlocal and coupled system for ϕ^{n+1}, ψ^{n+1}, and u^{n+1} in the scheme (3.10)-(3.13) that need costly iterative solvers to compute. But in practice, we can implement the scheme through the following decoupling procedure.

We first rewrite (3.12) as follows,

$$u^{n+1} = \frac{1}{2}\int_\Omega H^{*,n+1}\phi^{n+1}d\boldsymbol{x} + g^n, \tag{3.19}$$

where

$$g^n = \frac{4u^n-u^{n-1}}{3} - \frac{1}{2}\int_\Omega H^{*,n+1}\frac{4\phi^n-\phi^{n-1}}{3}d\boldsymbol{x}. \tag{3.20}$$

Then the scheme (3.10)-(3.11) can be combined together to be

$$\begin{aligned}\frac{3}{2M\delta t}\phi^{n+1} &- S\Delta\phi^{n+1} + \epsilon^2\Delta^2\phi^{n+1} + \alpha\epsilon^2(\phi^{n+1}-\bar{\phi}^{n+1})\\ &- \frac{1}{2}\Delta H^{*,n+1}\int_\Omega H^{*,n+1}\phi^{n+1}d\boldsymbol{x} = \tilde{g}^n,\end{aligned} \tag{3.21}$$

where $\tilde{g}^n$ is an explicit term defined as

$$\tilde{g}^n = \frac{4\phi^n-\phi^{n-1}}{2M\delta t} - S\Delta\phi^{*,n+1} + \Delta(g^n H^{*,n+1}). \tag{3.22}$$

By taking L^2 inner product of (3.21) with 1, we obtain the explicit formula for $\bar{\phi}^{n+1}$ that reads as

$$\bar{\phi}^{n+1} = \frac{2M\delta t}{3|\Omega|}\int_\Omega \tilde{g}^n d\boldsymbol{x}. \tag{3.23}$$

Thus (3.21) can be written as

$$\mathscr{P}(\phi^{n+1}) - \frac{1}{2}\Delta H^{*,n+1}\int_\Omega H^{*,n+1}\phi^{n+1}d\boldsymbol{x} = \widehat{g}^n, \tag{3.24}$$

where $\mathscr{P}(\cdot)$ is the linear operator that is defined as

$$\mathscr{P}(\psi) = (\frac{3}{2M\delta t} - S\Delta + \epsilon^2\Delta^2 + \alpha\epsilon^2)\psi, \tag{3.25}$$

and $\widehat{g}^n = \tilde{g}^n + \frac{2M\alpha\epsilon^2\delta t}{3|\Omega|}\int_\Omega \tilde{g}^n d\boldsymbol{x}$.

Define a linear operator $\mathscr{P}^{-1}(\cdot)$, such that for any periodic function $\phi \in L^2(\Omega)$, $\psi = \mathscr{P}^{-1}(\phi)$ is the solution of the following linear system

$$\mathscr{P}(\psi) = \phi, \tag{3.26}$$

with periodic boundary conditions. By applying the operator $\mathscr{P}^{-1}$ to (3.24), then we obtain

$$\phi^{n+1} - \frac{1}{2}\mathscr{P}^{-1}(\Delta H^{*,n+1})\int_\Omega H^{*,n+1}\phi^{n+1}d\boldsymbol{x} = \mathscr{P}^{-1}(\widehat{g}^n). \tag{3.27}$$

By taking the L^2 inner product of (3.27) with $H^{*,n+1}$, we obtain

$$\int\limits_{\Omega} H^{*,n+1}\phi^{n+1}d\boldsymbol{x} = \frac{\int_\Omega H^{*,n+1}\mathscr{P}^{-1}(\widehat{g}^n)d\boldsymbol{x}}{1-\frac{1}{2}\int_\Omega H^{*,n+1}\mathscr{P}^{-1}(\Delta H^{*,n+1})d\boldsymbol{x}}. \tag{3.28}$$

It is easy to check the term in the denominator $-\int_\Omega H^{*,n+1}\mathscr{P}^{-1}(\Delta H^{*,n+1})d\boldsymbol{x} \geq 0$ since $-\mathscr{P}^{-1}(\Delta)$ is a positive definite operator.

Furthermore, (3.28) actually provides an explicit formulation for the nonlocal term $\int_\Omega H^{*,n+1}\phi^{n+1}d\boldsymbol{x}$. Therefore, in computations, we first find $\psi_1 = \mathscr{P}^{-1}(\widehat{g}^n)$ and $\psi_2 = \mathscr{P}^{-1}(\Delta H^{*,n+1})$, that means to solve the following two decoupled, biharmonic equations,

$$(\frac{3}{2M\delta t} - S\Delta + \epsilon^2\Delta^2 + \alpha\epsilon^2)\psi_1 = \widehat{g}^n, \tag{3.29}$$

and

$$(\frac{3}{2M\delta t} - S\Delta + \epsilon^2\Delta^2 + \alpha\epsilon^2)\psi_2 = \Delta H^{*,n+1}, \tag{3.30}$$

with the periodic boundary conditions. And then, after by applying (3.28) to update $\int_\Omega H^{*,n+1}\phi^{n+1}d\boldsymbol{x}$, we can obtain ϕ^{n+1} from (3.27) directly.

To summarize, the nonlocal coupled scheme (3.10)-(3.13) can be easily implemented in the following manner:

- Compute ψ_1 and ψ_2 by solving two linear biharmonic equations with constant coefficients, (3.29) and (3.30);
- Compute $\int_\Omega H^{*,n+1}\phi^{n+1}d\boldsymbol{x}$ from (3.28) and update u^{n+1} from (3.19);
- Update ϕ^{n+1} from (3.27).

Hence, the total cost at each time step is essentially *solving two decoupled biharmonic equations with constant coefficients*. We note that these equations with periodic boundary conditions can be easily computed by the Fourier-Spectral method. Hence, this scheme is extremely efficient and easy to implement. We can also break the biharmonic equation into two elliptic equations so that the finite element method with lower order element can be used.

Now we prove the scheme (3.10)-(3.13) is unconditionally energy stable as follows.

Theorem 3.1. *The scheme* (3.10)-(3.13) *is unconditionally energy stable which satisfies the following discrete energy dissipation law,*

$$\frac{1}{\delta t}(E^{n+1}-E^n) \leq -M\|\nabla w^{n+1}\|^2 \leq 0, \tag{3.31}$$

where

$$\begin{aligned} E^{n+1} =& \frac{\epsilon^2}{2}(\frac{\|\nabla\phi^{n+1}\|^2 + \|2\nabla\phi^{n+1}-\nabla\phi^n\|^2}{2}) + \frac{\alpha\epsilon^2}{2}(\frac{\|\nabla\psi^{n+1}\|^2 + \|2\nabla\psi^{n+1}-\nabla\psi^n\|^2}{2}) \\ &+ \frac{(u^{n+1})^2 + (2u^{n+1}-u^n)^2}{2} + S\frac{\|\phi^{n+1}-\phi^n\|^2}{2}. \end{aligned} \tag{3.32}$$

Proof. By taking the L^2 inner product of (3.10) with $-2M\delta t w^{n+1}$, we obtain

$$-(3\phi^{n+1}-4\phi^n+\phi^{n-1}, w^{n+1}) = 2\delta t M\|\nabla w^{n+1}\|^2. \tag{3.33}$$

By taking the L^2 inner product of (3.11) with $3\phi^{n+1}-4\phi^n+\phi^{n-1}$, and using integration by parts, we obtain

$$\begin{aligned} (w^{n+1}, 3\phi^{n+1}-4\phi^n+\phi^{n-1}) =& \epsilon^2(\nabla\phi^{n+1}, 3\nabla\phi^{n+1}-4\nabla\phi^n+\nabla\phi^{n-1}) \\ &+ u^{n+1}(H^{*,n+1}, 3\phi^{n+1}-4\phi^n+\phi^{n-1}) \\ &+ S(\phi^{n+1}-2\phi^n+\phi^{n-1}, 3\phi^{n+1}-4\phi^n+\phi^{n-1}) \\ &+ \alpha\epsilon^2(\psi^{n+1}, 3\phi^{n+1}-4\phi^n+\phi^{n-1}). \end{aligned} \tag{3.34}$$

From (3.13), we can derive

$$-\Delta(3\psi^{n+1}-4\psi^n+\psi^{n-1}) = 3\phi^{n+1}-4\phi^n+\phi^{n-1}-(3\bar{\phi}^{n+1}-4\bar{\phi}^n+\bar{\phi}^{n-1}). \tag{3.35}$$

By taking the L^2 inner product of (3.35) with $\alpha\epsilon^2\psi^{n+1}$, we obtain

$$\alpha\epsilon^2(3\nabla\psi^{n+1}-4\nabla\psi^n+\nabla\psi^{n-1},\nabla\psi^{n+1})=\alpha\epsilon^2(3\phi^{n+1}-4\phi^n+\phi^{n-1},\psi^{n+1}), \tag{3.36}$$

where we use $(3\bar{\phi}^{n+1}-4\bar{\phi}^n+\bar{\phi}^{n-1},\psi^{n+1})=0$ since $\int_\Omega \psi^{n+1}d\boldsymbol{x}=0$.

By multiplying (3.12) with $-2u^{n+1}$, we obtain

$$-2(3u^{n+1}-4u^n+u^{n-1})u^{n+1}=-u^{n+1}\int\limits_\Omega H^{*,n+1}(3\phi^{n+1}-4\phi^n+\phi^{n-1})d\boldsymbol{x}. \tag{3.37}$$

Combining the above equations and applying the following two identities

$$\begin{aligned}&2a(3a-4b+c)=a^2+(2a-b)^2-b^2-(2b-c)^2+(a-2b+c)^2,\\&(3a-4b+c)(a-2b+c)=(a-b)^2-(b-c)^2+2(a-2b+c)^2,\end{aligned} \tag{3.38}$$

we obtain

$$\begin{aligned}&\frac{\epsilon^2}{2}(\|\nabla\phi^{n+1}\|^2+\|2\nabla\phi^{n+1}-\nabla\phi^n\|^2)-\frac{\epsilon^2}{2}(\|\nabla\phi^n\|^2+\|2\nabla\phi^n-\nabla\phi^{n-1}\|^2)\\&+\frac{\alpha\epsilon^2}{2}(\|\nabla\psi^{n+1}\|^2+\|2\nabla\psi^{n+1}-\nabla\psi^n\|^2)-\frac{\alpha\epsilon^2}{2}(\|\nabla\psi^n\|^2+\|2\nabla\psi^n-\nabla\psi^{n-1}\|^2)\\&+\Big((u^{n+1})^2+(2u^{n+1}-u^n)^2\Big)-\Big((u^n)^2+(2u^n-u^{n-1})^2\Big)\\&+S\|\phi^{n+1}-\phi^n\|^2-S\|\phi^n-\phi^{n-1}\|^2\\&+\frac{\epsilon^2}{2}\|\nabla\phi^{n+1}-2\nabla\phi^n+\nabla\phi^{n-1}\|^2+\frac{\alpha\epsilon^2}{2}\|\nabla\psi^{n+1}-2\nabla\psi^n+\nabla\psi^{n-1}\|^2\\&+(u^{n+1}-2u^n+u^{n-1})^2+2S\|\phi^{n+1}-2\phi^n+\phi^{n-1}\|^2=-2\delta tM\|\nabla\mu^{n+1}\|^2.\end{aligned}$$

Finally, we obtain the desired result after dropping some positive terms. □

Remark 3.3. Heuristically, $\frac{1}{\delta t}(E^{n+1}-E^n)$ is a second-order approximation of $\frac{d}{dt}E(u,\phi)$ at $t=t^{n+1}$. For any smooth variable ψ with time, we have

$$\begin{aligned}&\frac{\|\psi^{n+1}\|^2-\|2\psi^{n+1}-\psi^n\|^2}{2\delta t}-\frac{\|\psi^n\|^2-\|2\psi^n-\psi^{n-1}\|^2}{2\delta t}\\&\qquad\cong\frac{\|\psi^{n+2}\|^2-\|\psi^n\|^2}{2\delta t}+O(\delta t^2)\cong\frac{d}{dt}\|\psi(t^{n+1})\|^2+O(\delta t^2),\end{aligned} \tag{3.39}$$

and

$$\frac{\|\psi^{n+1}-\psi^n\|^2-\|\psi^n-\psi^{n-1}\|^2}{2\delta t}\cong O(\delta t^2). \tag{3.40}$$

Remark 3.4. It is straightforward to develop the second-order Crank-Nicolson scheme by using the same linear stabilization term. We omit the details to the interested readers since the proof of energy stability is quite similar to Theorem 3.1. The SAV type scheme is particularly suitable for the equations that is derived by the gradient flow approach as long as the total free energy is bounded from below. It is worthy to mention that the SAV or IEQ method can only ensure the stability of the modified energy instead of the original energy. In addition, although we consider only time discrete schemes in this study, the results can be carried over to any consistent finite-dimensional Galerkin approximations in the space since the proofs are all based on a variational formulation with all test functions in the same space as the space of the trial functions. Moreover, it is expected that optimal error estimates can be obtained without any essential difficulties since the H^1 bound for ϕ is satisfied naturally. We will implement the subsequent error analysis in the future work by following the same lines as the analytical work for isotropic Allen-Cahn/Cahn-Hilliard models in [24,34].

3.2. Other type schemes

In comparisons with the S-SAV scheme developed above, we also apply several other prevalent techniques to discretize the nonlinear terms, including the fully-implicit and convex splitting schemes listed below.

3.2.1. Fully-implicit scheme

The second-order fully-implicit scheme based on the BDF2 formula reads as follows.

$$\frac{3\phi^{n+1}-4\phi^n+\phi^{n-1}}{2M\delta t}=\Delta w^{n+1}, \tag{3.41}$$

$$w^{n+1}=-\epsilon^2\Delta\phi^{n+1}+f(\phi^{n+1})+\alpha\epsilon^2\psi^{n+1}, \tag{3.42}$$

$$\psi^{n+1}=-(\Delta^{-1})(\phi^{n+1}-\bar{\phi}^{n+1}). \tag{3.43}$$

About the detailed discussions about the stability, solvability for the fully-implicit scheme for the Cahn-Hilliard phase-field model without the nonlocal potential (i.e., $\alpha = 0$), we refer to [10,25]. It is expected similar arguments can be applied to the above scheme. The details are left to the interested readers.

3.2.2. Convex-splitting scheme

The second-order convex-splitting scheme based on Crank-Nicolson formula reads as follows.

$$\begin{cases} \dfrac{\phi^{n+1}-\phi^n}{M\delta t} = \Delta w^{n+\frac{1}{2}}, \\ w^{n+\frac{1}{2}} = -\epsilon^2 \Delta \phi^{n+\frac{1}{2}} + \dfrac{(\phi^{n+1})^2 + (\phi^n)^2}{2} \dfrac{\phi^{n+1}+\phi^n}{2} + \alpha\epsilon^2 \psi^{n+\frac{1}{2}}, \\ \psi^{n+\frac{1}{2}} = -(\Delta^{-1})(\phi^{n+\frac{1}{2}} - \bar{\phi}^{n+\frac{1}{2}}), \end{cases} \tag{3.44}$$

where $\phi^{n+\frac{1}{2}} = \frac{\phi^{n+1}+\phi^n}{2}$ and $\psi^{n+\frac{1}{2}} = \frac{\psi^{n+1}+\psi^n}{2}$. By using the similar approach given in [18,19], one can prove that the scheme is unconditionally energy stable. Thus we omit the detailed derivations of the energy stability proof in this paper.

4. Numerical simulation

In this section, we present a number of 2D and 3D numerical examples to demonstrate the accuracy, energy stability, and efficiency of the developed stabilized-SAV scheme (3.10)-(3.13). In all examples, we consider a computational domain $\Omega = [0, 2\pi]^d$, $d = 2, 3$ with periodic boundary conditions and we adopt the Fourier-spectral method to discretize the space.

If not explicitly specified, the default values of parameters are set as follows,

$$M = 1,\ \epsilon = 0.06,\ S = 2,\ B = 1, \alpha = 100. \tag{4.1}$$

4.1. Accuracy test

We first perform numerical simulations to test the convergence rates of the proposed stabilized-SAV scheme (3.10)-(3.13), denoted by S-SAV. For comparisons, we also compute the convergence rates by using the non-stabilized version of SAV scheme, i.e., scheme (3.10)-(3.13) but with $S = 0$, denoted by SAV; the fully-implicit scheme, denoted by Imp; and the convex-splitting scheme, denoted by CS. For the latter two nonlinear schemes, we use Newton iterative method to linearize the nonlinear system.

We perform refinement tests for temporal convergence by setting the initial condition of two circles as follows,

$$\phi(x, y, t = 0) = \frac{1}{4} \sum_{i=1}^{2} -\tanh\left(\frac{\sqrt{(x - x_i)^2 + (y - y_i)^2 - r_i}}{1.5\epsilon}\right) + \frac{3}{4}, \tag{4.2}$$

where $(x_1, y_1, r_1) = (\pi - 0.8, \pi, 1.4)$ and $(x_2, y_2, r_2) = (\pi + 1.7, \pi, 0.5)$. Since the exact solution is not known, we choose the solution obtained with the time step size $\delta t = 1\text{e–}9$ computed by the scheme S-SAV as the benchmark solution (approximately the exact solution) for computing errors. We discretize the space using $N_x = N_y = 129$ Fourier modes for x and y directions so that the errors from the spatial discretization are negligible compared to the temporal discretization errors. In Fig. 4.1-Fig. 4.3, we plot the L^2 errors of the phase variable between the numerical solution and the exact solution at $t = 0.2$ with different time step sizes by varying the mobility parameter M increasingly. Some observed features are listed as follows.

- First, in Fig. 4.1(a), we set $M = \epsilon$ and plot the errors computed by using all four schemes, S-SAV, SAV, CS, and Imp. We observe these schemes not only present the good convergence rate that almost perfectly matches the second-order accuracy for the time step but also good approximations to the exact solution, regardless of whether they are stabilized or not. Meanwhile, for fixed δt, the magnitude of errors is Imp<SAV<S-SAV< CS, since the stabilization term added in the scheme S-SAV actually increases the splitting errors. In Fig. 4.1(b), we plot the average number of iterations that these schemes need for each time step. We can see that the scheme S-SAV (or SAV) can significantly save the computational cost while using large time steps since they are free of iterations (we omit the plots of the scheme SAV in Fig. 4.1(b) since its computational cost is the same as that of S-SAV).
- Second, in Fig. 4.2(a), we set $M = 1$. We observe that, when $\delta t > 1.25\text{e–}3$, the non-stabilized scheme SAV totally loses the accuracy. When $\delta t \le 1.25\text{e–}3$, it can present good approximations and second-order accuracy. On the contrary, the other three schemes, S-SAV, CS, and Imp, are stable for all tested time steps and perform good approximations and corresponding orders of accuracy all along. The average number of iterations for each time step are also plotted in Fig. 4.2(b). The computational cost of the scheme S-SAV is quite low compared to the nonlinear schemes. For instances, when $\delta t = 0.01$, for each times step, the fully-implicit scheme needs around 500 times iterations, the convex-splitting scheme needs around 250 times, while the scheme S-SAV does not need any iterations at all.

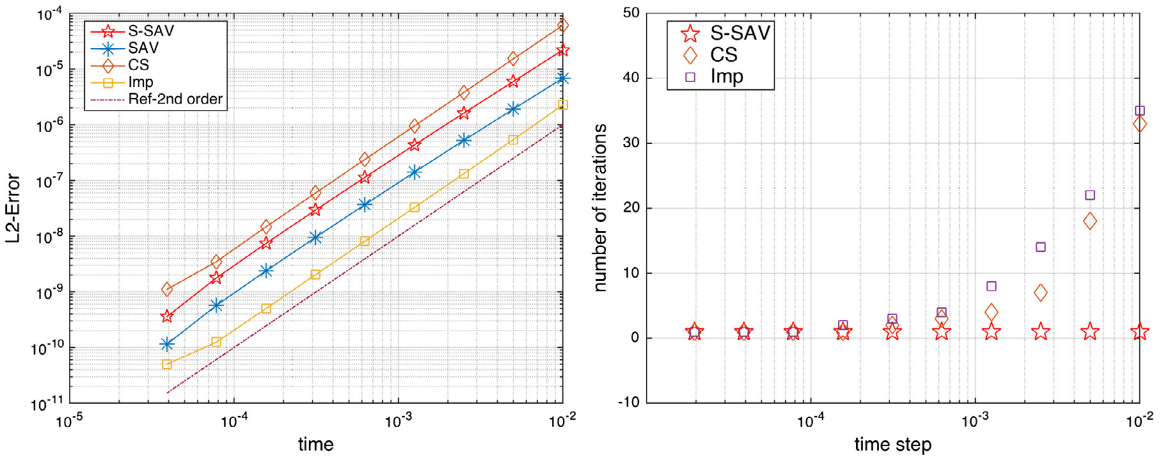

(a) $M = \epsilon$.

(b) Number of iterations with various δt.

Fig. 4.1. (a) The L^2 numerical errors for the phase field variable ϕ that are computed using the four schemes, S-SAV, SAV, CS, and Imp with various temporal resolutions with the mobility parameter $M = \epsilon$. (b) The average number of iterations that these schemes need for each time step (the plots of the scheme SAV is omitted here since its computational cost is the same as that of S-SAV).

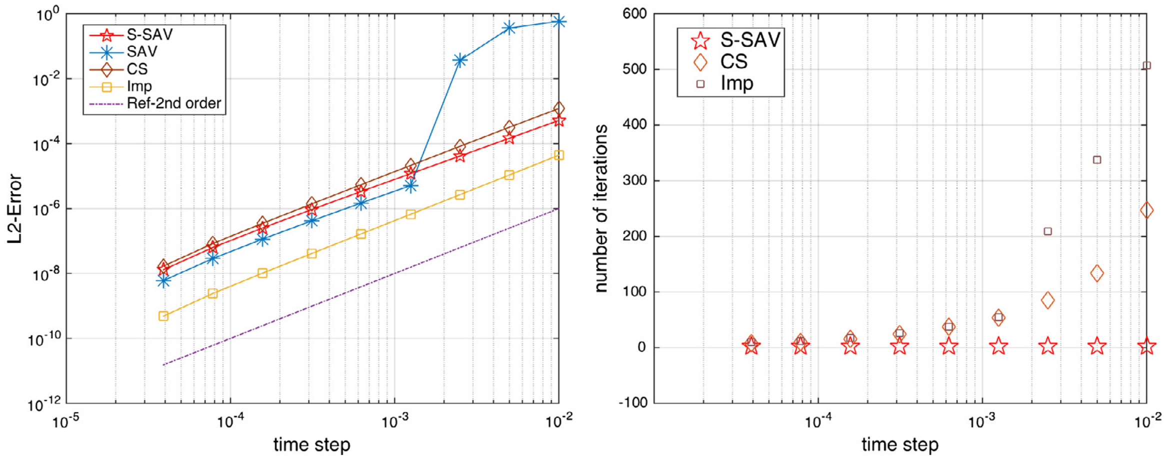

(a) $M = 1$.

(b) Number of iterations with various δt.

Fig. 4.2. (a) The L^2 numerical errors for the phase field variable ϕ that are computed using the four schemes, S-SAV, SAV, CS, and Imp with various temporal resolutions with the mobility parameter $M = 1$. (b) The average number of iterations that these schemes need for each time step.

- Finally, we set $M = \epsilon^{-2}$ and the errors are plotted in Fig. 4.3(a). We observe that the non-stabilized scheme SAV totally loses the accuracy for all tested time steps. When $\delta t \geq 7.8125\text{e}{-5}$, the scheme CS blows up quickly thus its error points are missing. The scheme Imp blows up for all tested time steps, thus its error points are missing as well. On the contrary, the stabilized scheme S-SAV is stable for all tested time steps and perform good approximations and corresponding orders of accuracy all along. The average number of iterations for the schemes S-SAV and CS for each time step is plotted in Fig. 4.3(b).

Therefore, through these numerical tests, we conclude that (i) if the mobility parameter is low, all schemes can solve the model well; (ii) if the mobility parameter is high, the stabilized scheme S-SAV overwhelmingly defeats all other three schemes from the stability and/or accuracy; and (iii) the scheme S-SAV overwhelmingly defeats the other two nonlinear schemes considering the computational cost.

We finally test the convergence rate for the spatial discretization for the S-SAV scheme. In Fig. 4.4(a) and (b), for three mobility parameters of $M = \epsilon$, 1, and ϵ^{-2}, we plot the L^2 errors of the phase field variable ϕ at time $t = 0.2$ by refining the grid points along the x and y directions, respectively. We use a very small time step $\delta t = 0.0001$ so that the errors from the temporal discretization are negligible compared to the spatial discretization errors. For the x-direction, we fix the number of Fourier modes $N_y = 257$ and vary the number of Fourier modes N_x starting from 33 with an increment of 32, with a

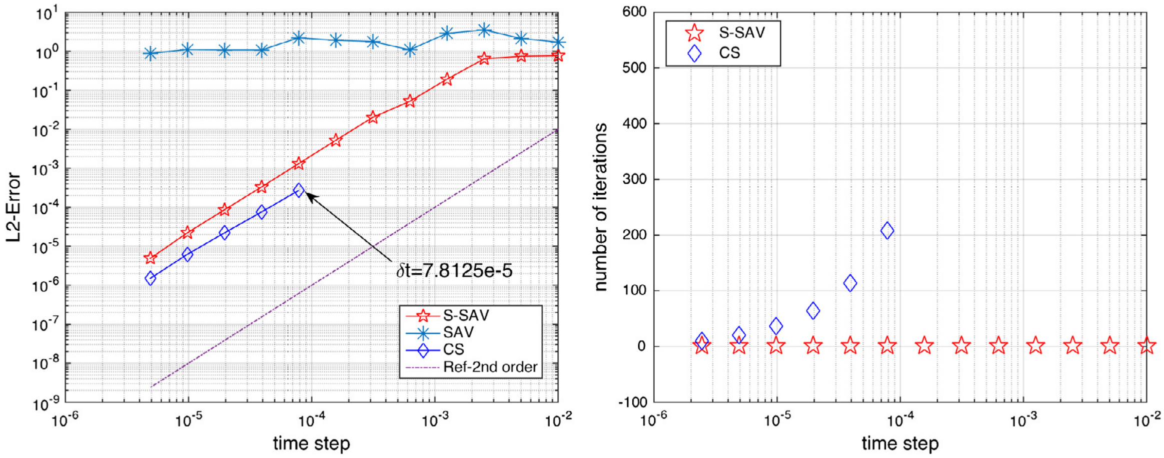

(a) $M = \epsilon^{-2}$.

(b) Number of iterations with various δt.

Fig. 4.3. (a) The L^2 numerical errors for the phase field variable ϕ that are computed using the three schemes, S-SAV, SAV, and CS with various temporal resolutions when the mobility parameter $M = \epsilon^{-2}$ (the scheme CS blows up quickly when $\delta t > 7.8125\text{e–}5$, thus its corresponding error points are missing; the scheme Imp blows up for all tested time steps, thus its error points are missing as well). (b) The average number of iterations that these schemes need for each time step.

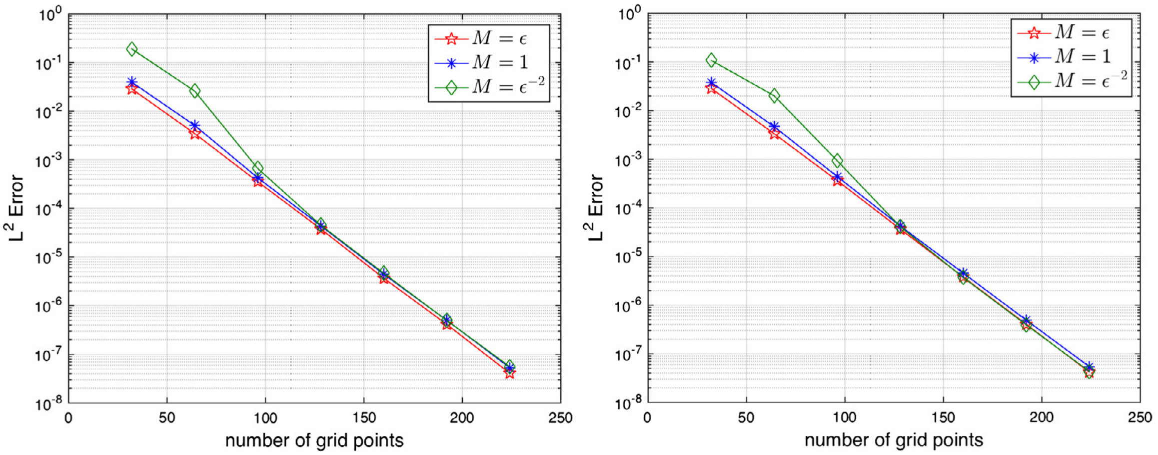

(a) Mesh refinement in x-direction.

(b) Mesh refinement in y-direction.

Fig. 4.4. (a) L^2 errors for mesh refinement tests in x-direction, (b) (a) L^2 errors for mesh refinement tests in y-direction. The L^2 numerical errors for ϕ that are computed using the scheme S-SAV with the initial condition is (4.2) and three mobility parameters $M = \epsilon, 1, \epsilon^{-2}$ are used.

reference solution obtained using the finest resolution of $N_x = N_y = 257$. The convergence in the y-direction is obtained in a similar way. We see that the S-SAV scheme achieves the spectral accuracy in the L^2 norm.

4.2. Evolution of two 2D circles

In this example, we investigate how the coarsening effect competes with the nonlocal Ohta-Kawasaki potential by using the scheme S-SAV and the initial condition of two circles given by (4.2). The time step is $\delta t = 0.001$ and the space is discretized using $N_x = N_y = 129$ Fourier modes. We vary the nonlocal parameter α and all other parameters are from (4.1).

In Fig. 4.5(a), we set $\alpha = 0$ which means the nonlocal effect vanishes and there exists only the coarsening effect. Snapshots of the profiles of the phase field variable ϕ are taken at $t = 0$, 1, 2, 5, and 10. We observe that the small circle is absorbed into the big circle, and the complete absorption happens around $t = 5$. In Fig. 4.5(b), we set $\alpha = 100$ and the snapshots of the profiles of the phase field variable ϕ are taken at $t = 0$, 10, 20, 40, and 100. We observe that the nonlocal effect dominates thus the coarsening effect is totally reversed where the volume of the big circle is continuously absorbed by the smaller one until these two circles finally form the peanut shape with equal volumes. In Fig. 4.5(c), we further in-

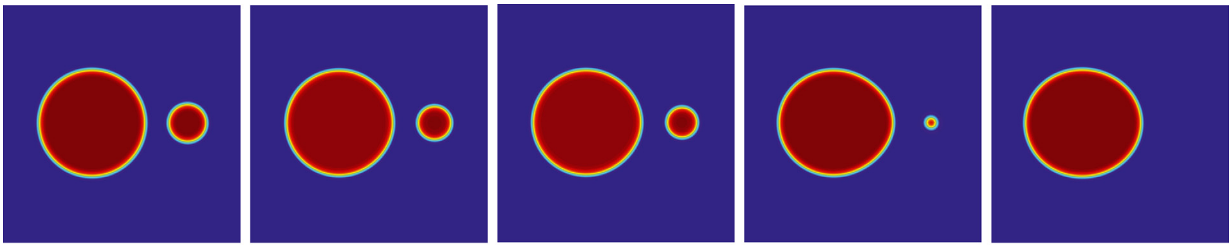

(a) Snapshots of ϕ at $t = 0$, 1, 2, 5, and 10 with $\alpha = 0$.

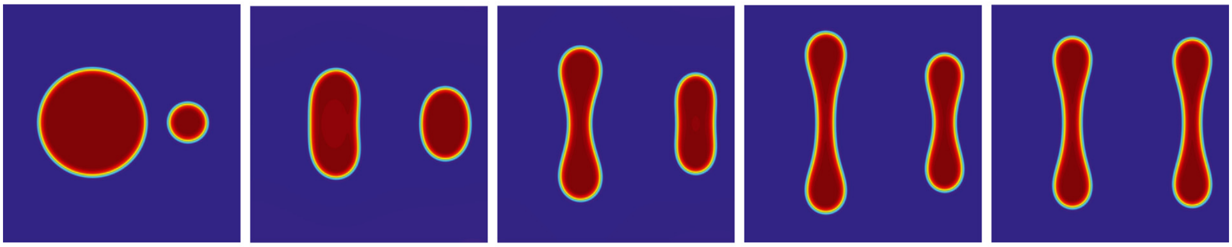

(b) Snapshots of ϕ at $t = 0$, 10, 20, 40, and 100 with $\alpha = 100$.

(c) Snapshots of ϕ at $t = 0$, 10, 20, 40, and 200 with $\alpha = 300$.

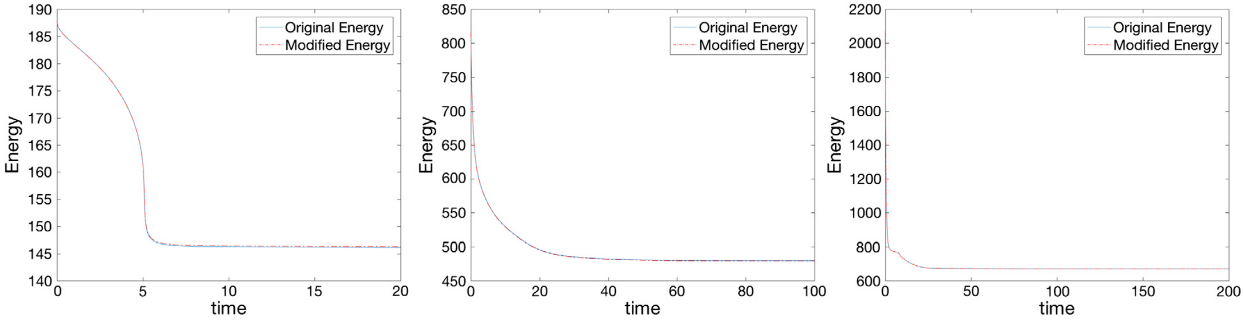

(d) Energy evolutions with time where $\alpha = 0$ (left), $\alpha = 100$ (middle), and $\alpha = 300$ (right).

Fig. 4.5. The dynamical evolutions of the phase variable ϕ with various nonlocal parameter α where (a) $\alpha = 0$, (b) $\alpha = 100$ and (c) $\alpha = 300$. (d) Time evolution of the two total free energy functionals, (2.16) and (3.2), with the three values of α.

crease the nonlocal effect by setting $\alpha = 300$. The snapshots of the profiles of the phase field variable ϕ are taken at $t = 0$, 10, 20, 40, and 200. While the small circle is forming the peanut shape, we observe that the big circle pinches off at the nearest position to the smaller one. Finally, both circles evolve into two elongated and bending peanut shapes with equal volumes.

In Fig. 4.5(d), for the above three cases, we plot time evolutions of the two total free energies, the original energy (2.16) and the modified energy (3.2), where these two energy curves are almost identical and they both decay monotonically at all times.

We further show the scheme S-SAV is unconditionally energy stable. In Fig. 4.6, we plot the evolution curves of the total free energy (2.16) computed by eight different time step sizes until $t = 10$ for $\alpha = 100$ and $\alpha = 300$, respectively. For all tested time steps, the obtained energy curves show the monotonic decays that confirms that the algorithm S-SAV is unconditionally stable. We also observe that, for $\delta t \le 0.0125$, the four energy curves coincide very well. But when $\delta t > 0.0125$, the energy curves deviate viewable away from others. This means the adopted time step size should not be larger than 0.0125, in order to get reasonably good accuracy (we set $\delta t = 0.001$ in the computations of Fig. 4.5).

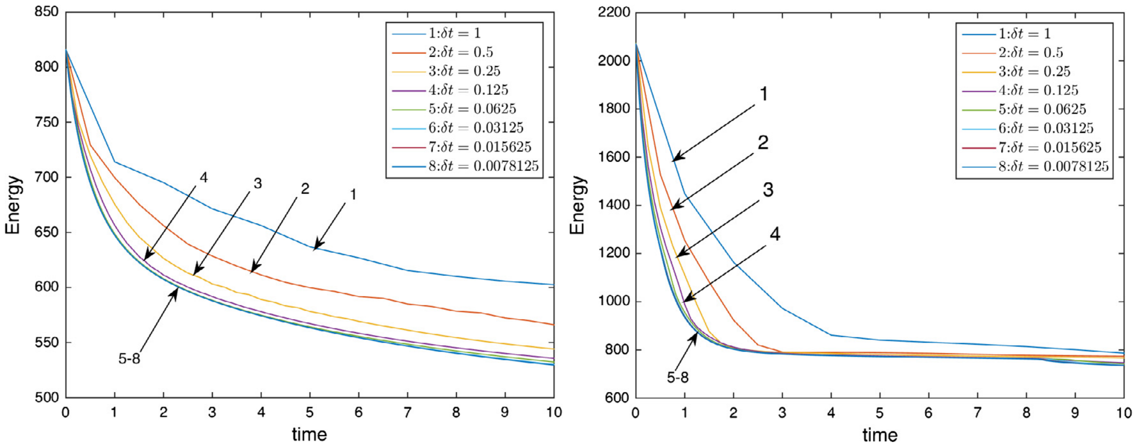

(a) $\alpha = 100$. (b) $\alpha = 300$.

Fig. 4.6. Time evolutions of the total free energy (2.16) computed by eight different time step sizes until $t = 10$ for (a) $\alpha = 100$ and (b) $\alpha = 300$. (For interpretation of the colors in the figure(s), the reader is referred to the web version of this article.)

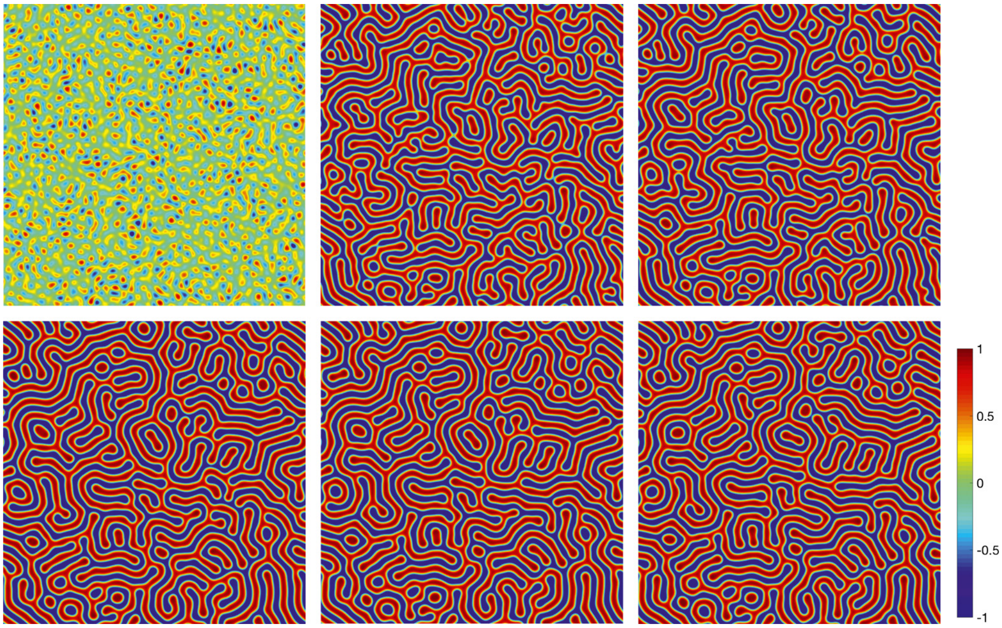

Fig. 4.7. The 2D dynamical evolution of the local volume fraction phase variable ϕ with the initial condition $\bar{\phi}_0 = 0$ and time step $\delta t = 0.001$. Snapshots of the numerical approximation are taken at $t = 0.04$, 0.2, 0.4, 2, 5, and 20.

4.3. Spinodal decomposition

In this example, we study the phase separation dynamics that is called spinodal decomposition using the developed scheme S-SAV. By considering a homogeneous binary mixture, the spontaneous growth of the concentration fluctuations can lead the system from the homogeneous to the two-phase state.

4.3.1. 2D case

We set the initial condition as the randomly perturbed concentration field as follows,

$$\phi(x, y, t = 0) = \bar{\phi}_0 + 0.001\text{rand}(x, y), \tag{4.3}$$

where the rand(x, y) is the random number in $[-1, 1]$ that follows the normal distribution. We use the scheme S-SAV with the time step $\delta t = 0.001$ and discretize the space using $N_x = N_y = 257$ Fourier modes. We set the parameters as $\alpha = 250000, \epsilon = 0.02, M = 1, S = 2, B = 1$.

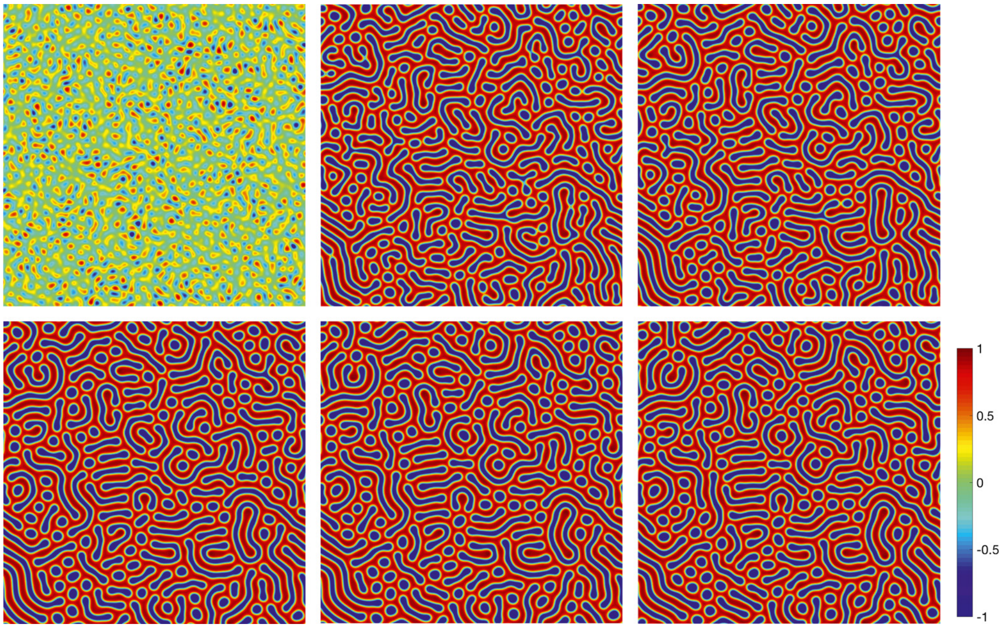

Fig. 4.8. The 2D dynamical evolution of the local volume fraction phase variable ϕ with the initial condition $\bar{\phi}_0 = 0.1$ and time step $\delta t = 0.001$. Snapshots of the numerical approximation are taken at $t = 0.04$, 0.2, 0.4, 2, 5, and 20.

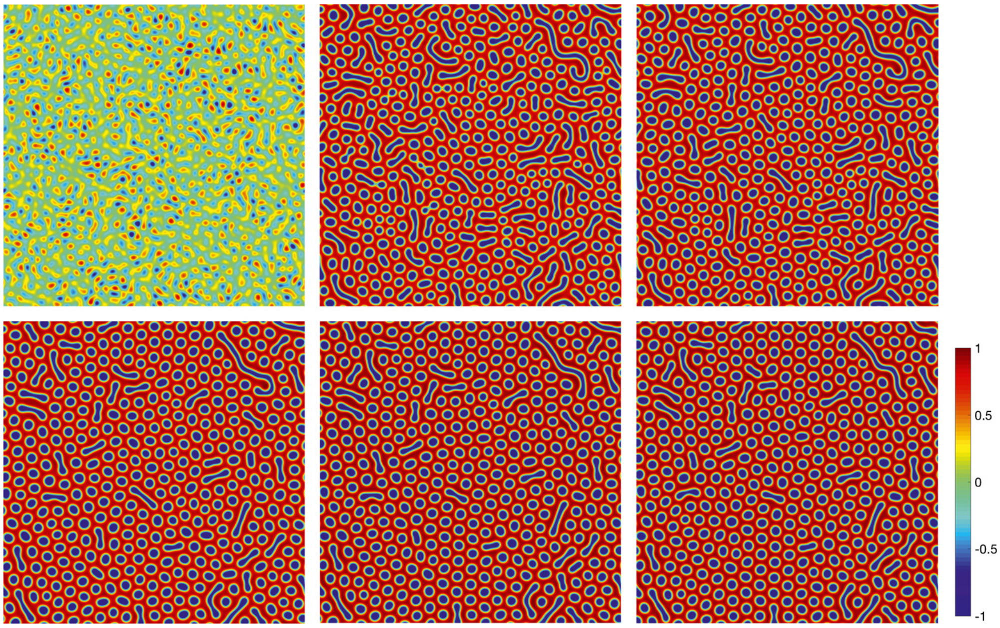

Fig. 4.9. The 2D dynamical evolution of the local volume fraction phase variable ϕ with the initial condition $\bar{\phi}_0 = 0.2$ and time step $\delta t = 0.001$. Snapshots of the numerical approximation are taken at $t = 0.04$, 0.2, 0.4, 2, 5, and 20.

In Fig. 4.7, we perform numerical simulations for the initial value $\bar{\phi}_0 = 0$ and snapshots of the phase field variable ϕ are taken at $t = 0.04$, 0.2, 0.4, 2, 5, and 20. We observe that the blue region is totally entangled with the red region, and the final equilibrium solution forms the cylindrical phase. In Fig. 4.8, we set $\bar{\phi}_0 = 0.1$. We observe that the final solution is quite different from the previous case. Although most of the blue region still graft and entangle with the red region, a small quantity of the blue region starts to form the BCC phase. The final equilibrium solution, shown at $t = 20$, is the co-existence of the cylindrical and BCC phases but the former phase dominates obviously. When the initial value is $\bar{\phi}_0 = 0.2$, in Fig. 4.9, we observe that more blue regions form the BCC phase and a small quantity of it still forms the cylindrical phase. The final equilibrium solution, shown at $t = 20$, is the co-existence of the cylindrical and BCC phases but the latter phase dominates.

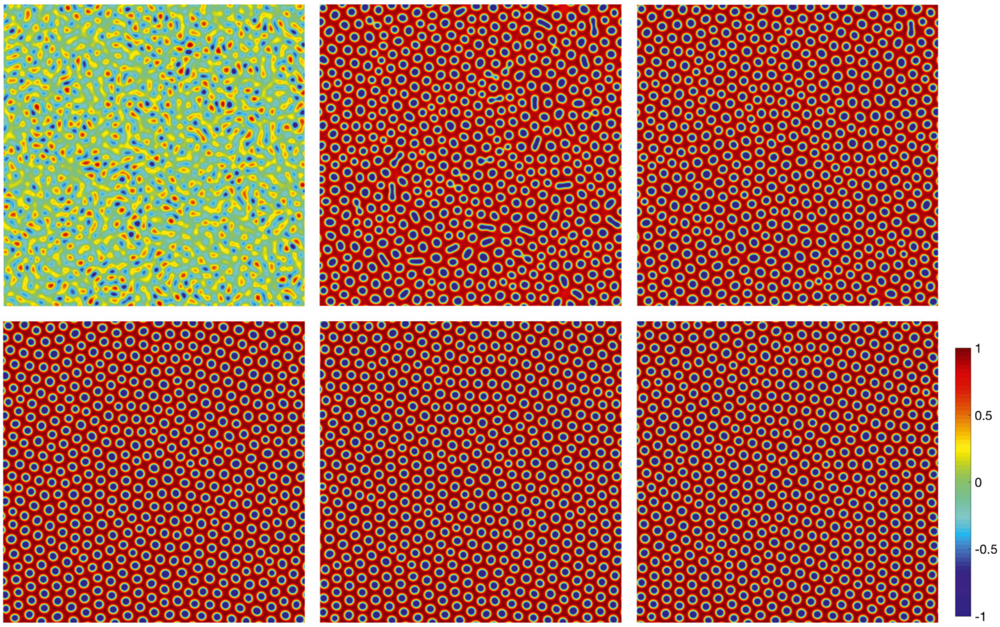

Fig. 4.10. The 2D dynamical evolution of the local volume fraction phase variable ϕ with the initial condition $\bar{\phi}_0 = 0.3$ and time step $\delta t = 0.001$. Snapshots of the numerical approximation are taken at $t = 0.04$, 0.2, 0.4, 2, 5, and 20.

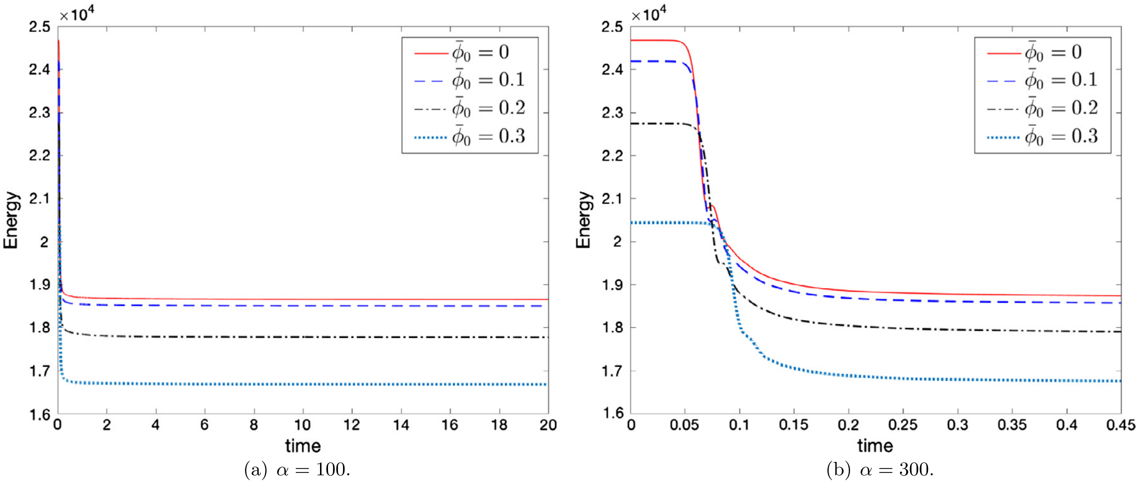

(a) $\alpha = 100$. (b) $\alpha = 300$.

Fig. 4.11. (a) Time evolution of the total free energy functional (2.16) for the spinodal decomposition examples with three different initial values of $\bar{\phi}_0 = 0$, 0.1, 0.2, and 0.3 in (4.3). (b) A close-up view for $t \in [0, 0.45]$.

Finally, we set $\bar{\phi}_0 = 0.3$ in Fig. 4.10. We then observe that a small quantity of cylindrical phase initially appears and turns to the BCC phase immediately. Thus the final equilibrium solution is the pure BCC phase in the whole domain.

In Fig. 4.11, we present the evolution of the total free energy functional (2.16) for all four initial conditions $\bar{\phi}_0 = 0$, 0.1, 0.2, and 0.3. The energy curves show the decays with the time that confirms that the scheme S-SAV is unconditionally stable.

4.3.2. 3D case

We further perform the 3D simulation where the initial condition is set as follows,

$$\phi(x, y, z, t = 0) = \bar{\phi}_0 + 0.001\mathrm{rand}(x, y, z), \tag{4.4}$$

where the rand(x, y, z) is the random number in $[-1, 1]$ that follows the normal distribution. We use the scheme S-SAV with the time step $\delta t = 0.001$ and discretize the space using $N_x = N_y = N_z = 129$ Fourier modes. We set the parameters as $\alpha = 10000$, $\epsilon = 0.05$, $M = 1$, $S = 2$, $B = 1$.

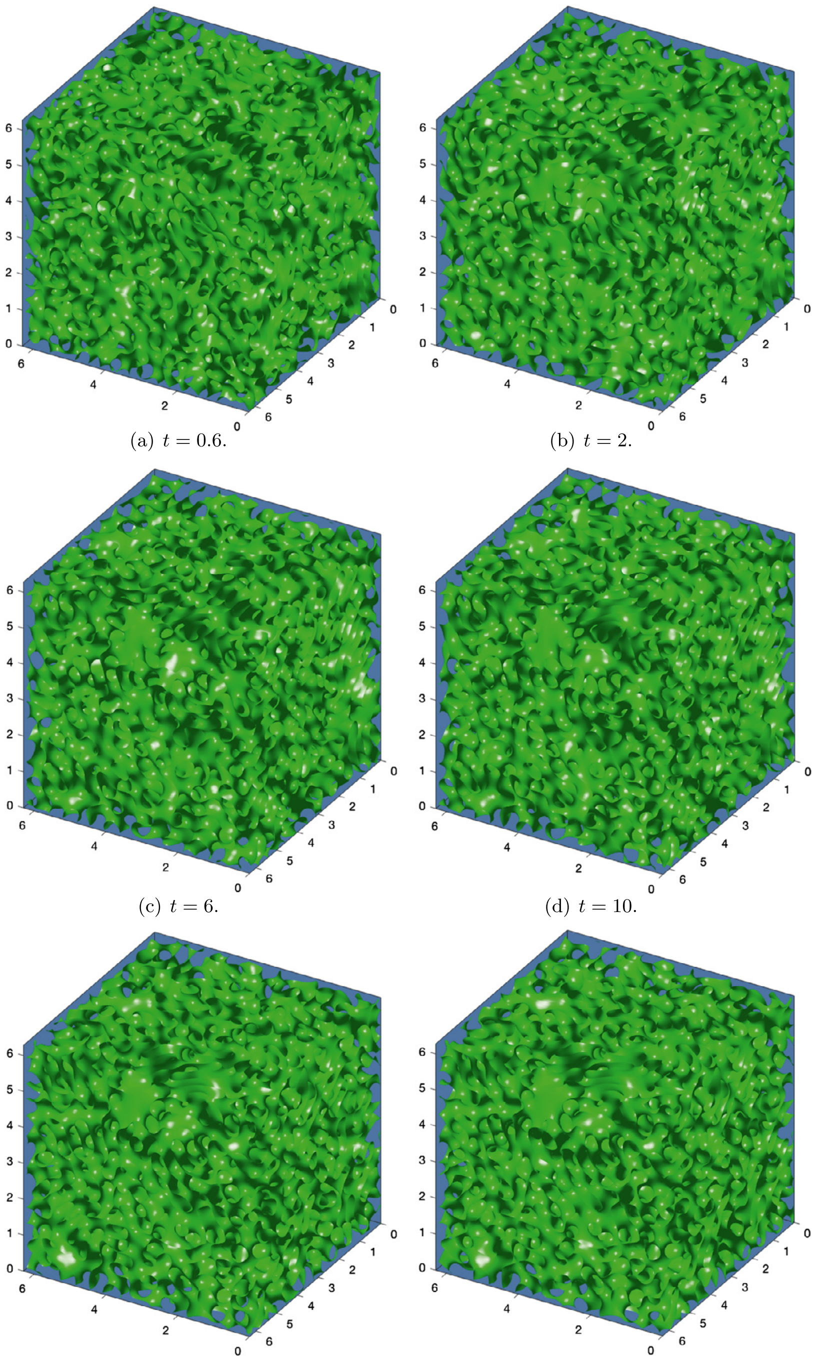

(a) $t = 0.6$. (b) $t = 2$. (c) $t = 6$. (d) $t = 10$. (e) $t = 50$. (f) $t = 80$.

Fig. 4.12. The 3D dynamical evolution of the isosurface of the phase variable ϕ with the initial condition $\bar{\phi}_0 = 0$ and time step $\delta t = 0.001$. Snapshots of the numerical approximation are taken at $t = 0.6$, 2, 6, 10, 50, and 80.

In Fig. 4.12 with the initial value $\bar{\phi}_0 = 0$, the dynamical behaviors of the phase field variable ϕ are shown in which the isosurfaces of $\{\phi(x, y, z) = 0\}$ are plotted at various times. We observe that the final equilibrium solution forms the gyroidal shape. By increasing the $\bar{\phi}_0$ to 0.2 in Fig. 4.13, the obtained final equilibrium solution presents the gyroidal shape but with a small quantity of spherical shape. In Fig. 4.14 with $\bar{\phi}_0 = 0.4$, we find that the final equilibrium solution presents the spherical shape in the whole domain. In order to obtain a more accurate view, we present the views through different cut-off planes for the equilibrium solutions in Fig. 4.15. It is quite clear that these equilibrium solutions actually present three different phases, i.e., gyroidal phase ($\bar{\phi}_0 = 0$), gyroidal-spherical mixed phase ($\bar{\phi}_0 = 0.2$), and spherical phase ($\bar{\phi}_0 = 0.4$).

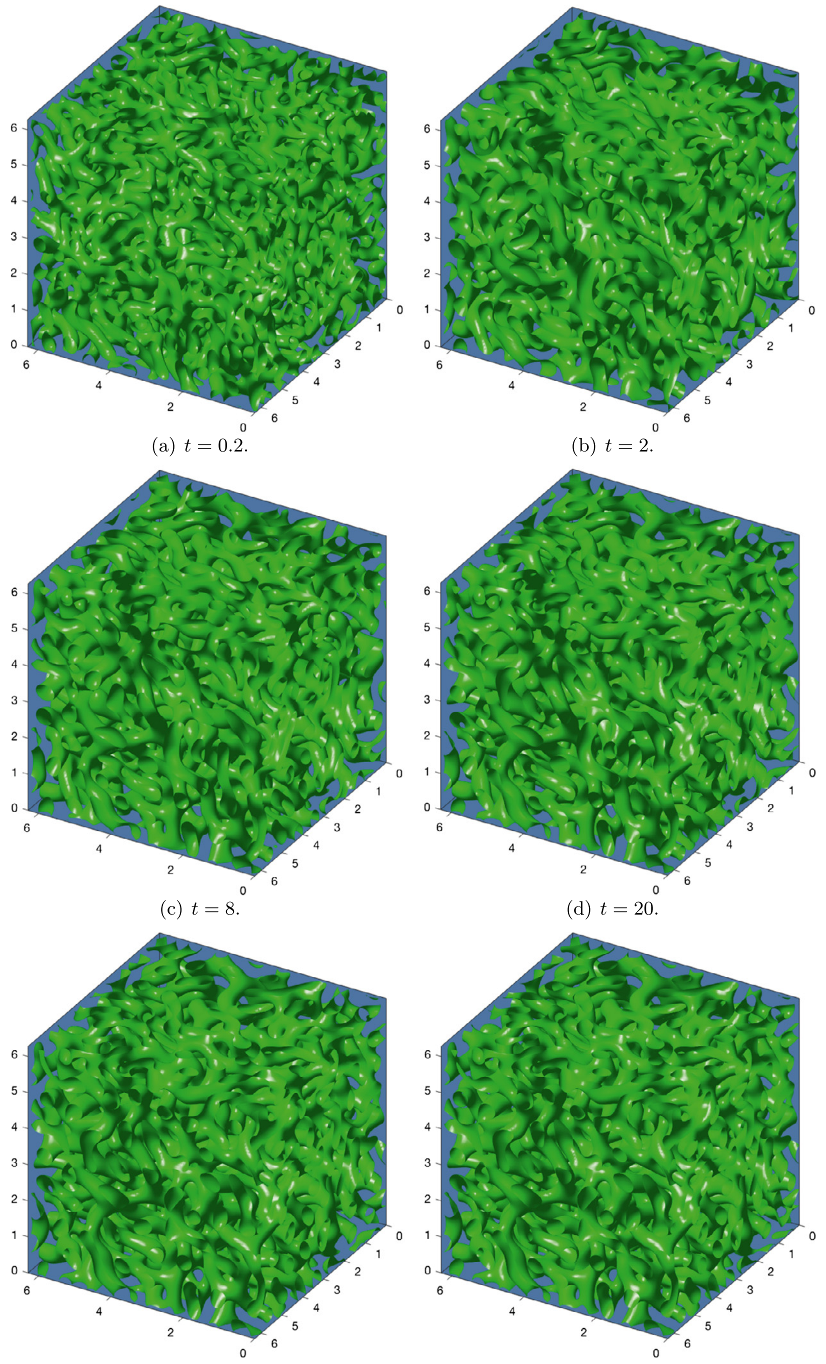

(a) $t = 0.2$. (b) $t = 2$.

(c) $t = 8$. (d) $t = 20$.

(e) $t = 60$. (f) $t = 80$.

Fig. 4.13. The 3D dynamical evolution of the isosurface of the phase variable ϕ with the initial condition $\bar{\phi}_0 = 0.2$ and time step $\delta t = 0.001$. Snapshots of the numerical approximation are taken at $t = 0.2$, 2, 8, 20, 60, and 80.

5. Concluding remarks

In this paper, we have developed a semi-discrete in time, easy-to-implement, fast, and second-order scheme for solving the Cahn-Hilliard phase field model for Diblock copolymers. The novelty of the proposed stabilized-SAV scheme is that iterations are successfully avoided in an artful manner, and one only needs to solve two biharmonic equations at each time step. The added linear stabilization term is shown to be crucial to enhancing the stability and keeping the required accuracy while using large time steps. We further prove the unconditional energy stability of the developed scheme rigorously.

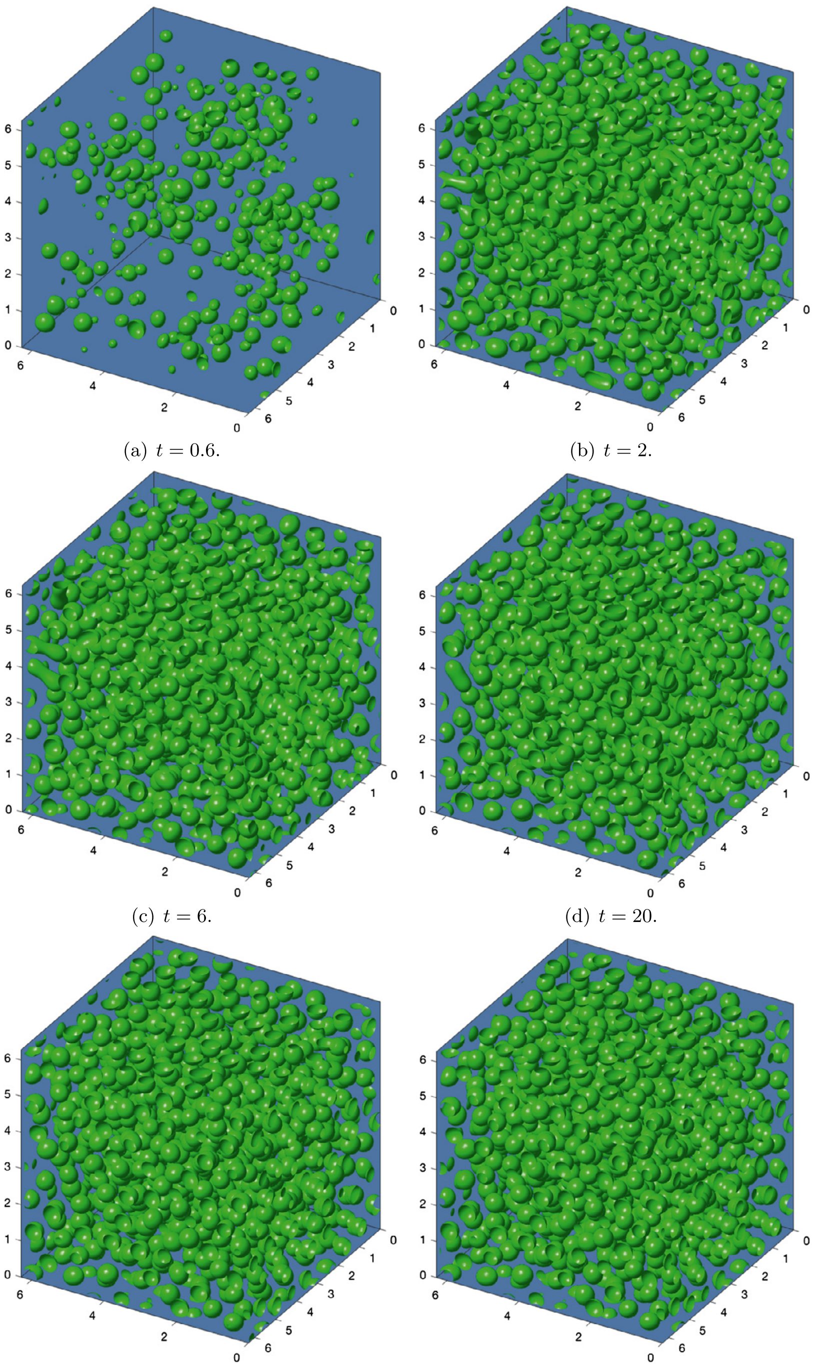

(a) $t = 0.6$. (b) $t = 2$.

(c) $t = 6$. (d) $t = 20$.

(e) $t = 40$. (f) $t = 80$.

Fig. 4.14. The 3D dynamical evolution of the local volume fraction phase variable ϕ with the initial condition $\bar{\phi}_0 = 0.4$ and time step $\delta t = 0.001$. Snapshots of the numerical approximation are taken at $t = 0.6$, 2, 6, 20, 40, and 80.

Through the comparisons with some other prevalent schemes like the non-stabilized SAV, fully-implicit, and convex-splitting schemes for some benchmark numerical examples in 2D and 3D, we demonstrate the stability and the accuracy of the developed scheme numerically.

Acknowledgements

The work of Jun Zhang is supported by the NSFC (No. 11901132), Guizhou Key Laboratory of Big Data Statistics Analysis (No. BDSA20190101) and the China Scholarship Council (No. 201908525061). C. Chen was partially supported by Natural

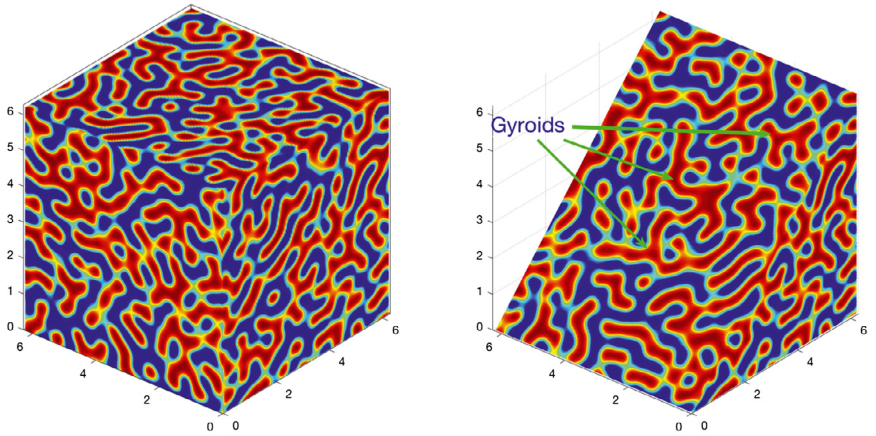

(a) $\bar{\phi}_0 = 0$.

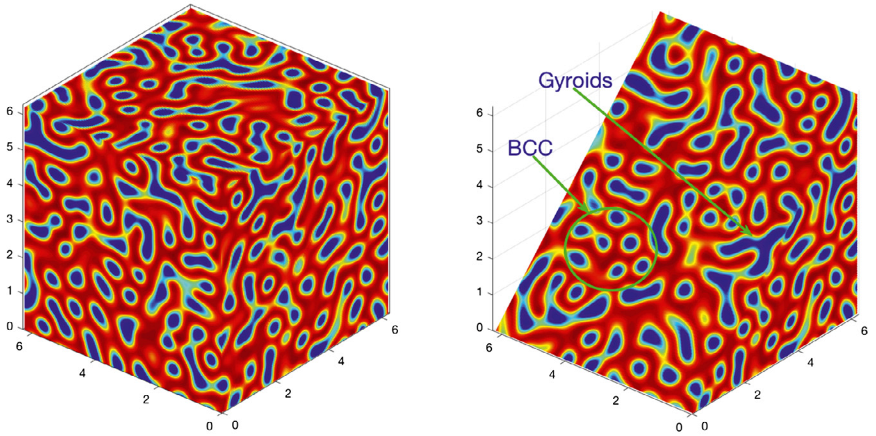

(b) $\bar{\phi}_0 = 0.2$.

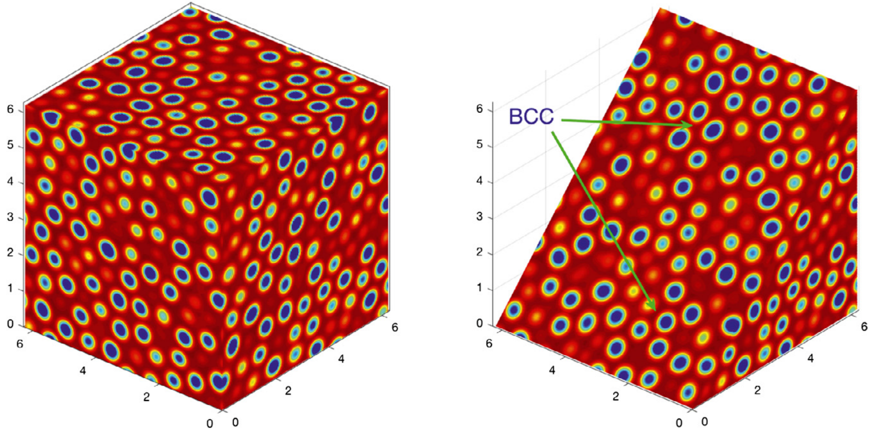

(c) $\bar{\phi}_0 = 0.4$.

Fig. 4.15. The 3D cut-off planes of the equilibrium solutions computed by using initial values of $\bar{\phi}_0 = 0$, 0.2, and 0.4. For each subfigure, the left one is the three horizontal/vertical cut-off planes, and the right one is the tilted cut-off plane.

Science Foundation of China (11771375 and 11571297). X. Yang was partially supported by National Science Foundation with grant numbers DMS (1720212 and 1818783).

References

[1] K. Binder, Collective diffusion, nucleation, and spinodal decomposition in polymer mixtures, J. Chem. Phys. 79 (1983) 6387.
[2] S.A. Brazovskii, Phase transition of an isotropic system to a nonuniform state, J. Exp. Theor. Phys. 41 (1) (1975) 85.
[3] C. Chen, X. Yang, Efficient numerical scheme for a dendritic solidification phase field model with melt convection, J. Comput. Phys. 388 (2019) 41–62.

[4] C. Chen, X. Yang, Fast, provably unconditionally energy stable, and second-order accurate algorithms for the anisotropic Cahn-Hilliard model, Comput. Methods Appl. Mech. Eng. 351 (2019) 35–59.
[5] Q. Cheng, J. Shen, Multiple scalar auxiliary variable (MSAV) approach and its application to the phase-field vesicle membrane model, SIAM J. Sci. Comput. 40 (2018) A3982–A4006.
[6] R. Choksi, X. Ren, On the derivation of a density functional theory for microphase separation of diblock copolymers, J. Stat. Phys. 113 (2003) 151–176.
[7] P.G. de Gennes, Scaling Concepts in Polymer Physics, Cornell University Press, Ithaca, 1979.
[8] P.G. de Gennes, Dynamics of fluctuations and spinodal decomposition in polymer blends, J. Chem. Phys. 7 (1980) 4756.
[9] D.J. Eyre, Unconditionally gradient stable time marching the Cahn-Hilliard equation, in: Computational and Mathematical Models of Microstructural Evolution, San Francisco, CA, 1998, in: Mater. Res. Soc. Sympos. Proc., vol. 529, MRS, Warrendale, PA, 1998, pp. 39–46.
[10] X. Feng, A. Prol, Numerical analysis of the Allen-Cahn equation and approximation for mean curvature flows, Numer. Math. 94 (2003) 33–65.
[11] M. Fialkowski, R. Holyst, Dynamics of phase separation in polymer blends revisited: morphology, spinodal, noise, and nucleation, Macromol. Theory Simul. 17 (2008) 263.
[12] G.H. Fredrickson, Surface ordering phenomena in block copolymer melts, Macromolecules 20 (6) (1987) 2535–2542.
[13] Y. Gao, X. He, L. Mei, X. Yang, Decoupled, linear, and energy stable finite element method for Cahn-Hilliard-Navier-Stokes-Darcy phase field model, SIAM J. Sci. Comput. 40 (2018) B110–B137.
[14] H. Gomez, T.J.R. Hughes, Provably unconditionally stable, second-order time-accurate, mixed variational methods for phase-field models, J. Comput. Phys. 230 (2011) 5310–5327.
[15] H. Gomez, Kristoffer G. van der Zee, Computational phase-field modeling, in: Encyclopedia of Computational Mechanics, second edition, John Wiley & Sons, Ltd, ISBN 978-1-119-00379-3, 2017.
[16] H. Gomez, V.M. Calo, Y. Bazilevs, T.J.R. Hughes, Isogeometric analysis of the Cahn-Hilliard phase-field model, Comput. Methods Appl. Mech. Eng. 197 (2008) 4333–4352.
[17] I.W. Hamley, Ordering in thin films of block copolymers: fundamentals to potential applications, Prog. Polym. Sci. 34 (2009) 1161–1210.
[18] D. Han, X. Wang, A second order in time, uniquely solvable, unconditionally stable numerical scheme for Cahn-Hilliard-Navier-Stokes equation, J. Comput. Phys. 290 (2015) 139–156.
[19] D. Han, A. Brylev, X. Yang, Z. Tan, Numerical analysis of second order, fully discrete energy stable schemes for phase field models of two phase incompressible flows, J. Sci. Comput. 70 (2017) 965–989.
[20] Q. Huang, X. Yang, X. He, Numerical approximations for a smectic–a liquid crystal flow model: first-order, linear, decoupled and energy stable schemes, Discrete Contin. Dyn. Syst., Ser. B 23 (2018) 2177–2192.
[21] T. Ohta, K. Kawasaki, Equilibrium morphology of block copolymer melts, Macromolecules 19 (10) (1986) 2621–2632.
[22] C. Overberger, Copolymerization: 1. general remarks; 2: selective examples of copolymerizations, J. Polym. Sci., Polym. Symp. 72 (1985) 67–69.
[23] I. Romero, Thermodynamically consistent time stepping algorithms for nonlinear thermomechanical systems, Int. J. Numer. Methods Eng. 79 (2009) 706–732.
[24] J. Shen, J. Xu, Convergence and error analysis for the scalar auxiliary variable (sav) schemes to gradient flows, SIAM J. Numer. Anal. 56 (2019) 2895–2912.
[25] J. Shen, X. Yang, Numerical approximations of Allen-Cahn and Cahn-Hilliard equations, Discrete Contin. Dyn. Syst., Ser. A 28 (2010) 1669–1691.
[26] J. Shen, C. Wang, S. Wang, X. Wang, Second-order convex splitting schemes for gradient flows with Ehrlich-Schwoebel type energy: application to thin film epitaxy, SIAM J. Numer. Anal. 50 (1) (2012) 105–125.
[27] J. Shen, J. Xue, J. Yang, The scalar auxiliary variable (sav) approach for gradient flows, J. Comput. Phys. 353 (2018) 407–416.
[28] X.-F. Wu, Y.A. Dzenis, Phase-field modeling of the formation of lamellar nanostructures in diblock copolymer thin films under inplanar electric fields, Phys. Rev. E 77 (3) (2008) 031807.
[29] C. Xu, C. Chen, X. Yang, X. He, Numerical approximations for the hydrodynamics coupled binary surfactant phase field model: second-order, linear, unconditionally energy stable schemes, Commun. Math. Sci. 17 (2019) 835–858.
[30] T. Xu, A.V. Zvelindovsky, G.J.A. Sevink, O. Gang, B. Ocko, Y. Zhu, S.P. Gido, T.P. Russell, Electric field induced sphere-to-cylinder transition in diblock copolymer thin films, Macromolecules 37 (18) (2004) 6980–6984.
[31] X. Yang, Linear first and second order and unconditionally energy stable numerical schemes for the phase field model of homopolymer blends, J. Comput. Phys. 327 (2016) 294–316.
[32] X. Yang, Numerical approximations for the Cahn-Hilliard phase field model of the binary fluid-surfactant system, J. Sci. Comput. 74 (2017) 1533–1553.
[33] X. Yang, Efficient linear, stabilized, second order time marching schemes for an anisotropic phase field dendritic crystal growth model, Comput. Methods Appl. Mech. Eng. 347 (2019) 316–339.
[34] X. Yang, G-D. Zhang, Numerical approximations of the Cahn-Hilliard and Allen-Cahn equations with general nonlinear potential using the invariant energy quadratization approach, arXiv:1712.02760, 2018, submitted for publication.
[35] X. Yang, J. Zhao, Q. Wang, J. Shen, Numerical approximations for a three components Cahn-Hilliard phase-field model based on the invariant energy quadratization method, Math. Models Methods Appl. Sci. 27 (2017) 1993–2030.
[36] J. Zhang, C. Chen, X. Yang, A novel decoupled and stable scheme for an anisotropic phase-field dendritic crystal growth model, Appl. Math. Lett. 95 (2019) 122–129.
[37] J. Zhao, X. Yang, Y. Gong, Q. Wang, A novel linear second order unconditionally energy stable scheme for a hydrodynamic Q-tensor model of liquid crystals, Comput. Methods Appl. Mech. Eng. 318 (2017) 803–825.